Estimation of the Melting Threshold of Ti Supersaturated Si Using Time Resolved Reflectometry and Haze Measurements

D. Montero, D. Caudevilla, S. Algaidy, R. Garcia-Hernansanz, A. Suler, P. Acosta-Alba, S. Kerdiles, D. Pastor, E. Garcia-Hemme, F. Roy, J. Olea.*

Dr. D. Montero, D. Caudevilla, S. Algaidy, Dr. R. Garcia-Hernansanz, Dr. D. Pastor, Dr. E. Garcia-Hemme, Dr. J. Olea

Thin Films and Microelectronics Group, Universidad Complutense de Madrid (UCM), Plaza de Ciencias 1 Madrid, 28040, Spain

E-mail: danielmontero@ucm.es

Dr. D. Montero, Dr. A. Suler, Dr. F. Roy

Digital Front-End Manufacturing & Technology, STMicroelectronics, Rue Jean Monnet 850 Crolles Cedex, F-38920, France

Dr. P. Acosta-Alba, Dr. S. Kerdiles
Université Grenoble Alpes, CEA, LETI, MINATEC Campus, 17 rue des Martyrs, Grenoble Cedex 9, F-38054, France

Keywords: nanosecond laser annealing, silicon supersaturation, silicon recrystallization, Time-Resolved Reflectometry, Haze measurements

1. Abstract

Hyperdoped or supersaturated semiconductors are gathering the attention of industry and research institutions due to their sub-bandgap photon absorption properties. In this study, two fast and non-invasive techniques, Time-Resolved Reflectometry (TRR) and Haze Measurements, are applied to infer the melt and solidification regimes of Ti supersaturated 300 mm silicon wafers, aiming to ease the characterization process towards high volume manufacturing of supersaturated materials. Ti supersaturation is attained by using an ion implantation process with a dose $3x10^{15}$ cm^{-2}, which amorphizes the surface. Crystalline quality is then recovered by means of a XeCl UV Nanosecond Laser Annealing (NLA) process. TRR technique is used to determine two different

melting and solidification processes of the laser annealed implanted surface. A first brief, low temperature peak (α peak) is associated with the melting process of the amorphized surface, followed by a longer peak/plateau (β_1 peak/plateau), linked to the melting process of the crystalline phase below the amorphized layer, at sufficiently high laser fluences. Haze technique is used to indirectly measure the crystalline quality after the solidification process of the laser-annealed surface. Atomic Force Microscopy (AFM) measurements are used to obtain the surface roughness value and cross-section HRTEM micrographs to check crystalline quality.

2. Introduction

Nanosecond Laser Annealing (NLA) or Pulsed Laser Melting (PLM) techniques are used to selectively heat up or even melt the first hundreds of nanometers of a semiconductor. Although there is a wide range of applications in the sub-melt regime [1,2], this manuscript deals with the melting process that occurs when the laser energy density reaches or surpasses the melting threshold of the semiconductor.

Dopant activation by NLA processes involving UV laser radiation have aroused great interest in the past decades [3]. The NLA process allows to selectively heat up the surface, without affecting the bulk of the sample, as energy is absorbed in the first hundreds of nanometers. The laser process can also be masked, providing area-selective annealing processes. Furthermore, the melting and solidification processes are faster than in conventional techniques, which allows for a significant reduction of the heat diffusion, allowing the dopant redistribution profiles to be shallower and steeper. This feature is particularly interesting for activating the dopants in the drain and source of MOS transistors [4]. In the case of shallow dopants in Si, extensive research has been conducted [2,5–9]. The use of NLA processes on Si substrates containing deep centers has also been studied by several research groups, for example, using titanium [10–13], vanadium [14,15], gold [16], tellurium [17,18], selenium [19] or sulfur [20,21]. Ti supersaturated Si is chosen in this study.

There has been an increased interest in the past years about modifying intrinsic Si properties by introducing a soaring concentration of deep centers (several orders of magnitude higher than the solid solubility limit), also known as supersaturating or hyperdoping Si [17,19,22]. The aim of supersaturating is to extend Si responsivity at energies below the band gap. Deep centers in semiconductors typically drop down the carrier lifetime as they act as generation-recombination centers. However, if the deep center concentration is higher than the Mott limit [23], a third band related to the deep impurities, different than the valence or the conduction band, may be formed. By choosing the appropriate host semiconductor and impurity, the position of this impurity band could lie between both bands. In this case, the carriers could promote from the valence to the conduction band by absorbing two photons of energy lower than the bandgap, in two different absorption processes, using the third band as an intermediate step. This band is usually referred to as the Intermediate Band (IB) in the literature [24]. Thus, supersaturated Si could be used to improve the sensitivity of Si in the sub-bandgap region, at wavelengths longer than 1.1 μm at room temperature. The interest to extend Si responsivity lies in the wide range of IR sensing applications that are poorly covered by currently available technology. In most cases, the materials used are rare, potentially contaminant or expensive [25]. Furthermore, they are not easily integrated within a CMOS route at sufficiently low cost [26]. Among all the possible applications, near IR sensing for smart driving applications, outdoor night vision or fiber optic telecommunications are highlighted.

Sub-bandgap response at room temperature has already been demonstrated in Si using Ti as deep centers [27], in concentrations high enough to induce the formation of a supersaturated Si layer, extending Si responsivity up to 2.5 μm wavelength at room temperature [28,29]. This work describes the use of two non-invasive, fast and reliable techniques, as Time-Resolved Reflectometry and Haze measurements, to study the effect of different laser annealing energy densities on the recrystallization process of Ti supersaturated Si layers. It is important to note that both non-destructive and non-contact techniques are performed at wafer level in 300 mm commercially available tools. In order to make these materials industrially scalable towards high volume manufacturing, wafer level characterization

techniques are preferred to speed up the characterization and optimization process, saving time and cost during the whole development process.

A XeCl excimer laser with relatively long pulse duration, around 150 ns, has been chosen to recover the crystal quality, as opposed to the shorter laser pulse duration usually found in other works that covered the supersaturation of Si substrates [12,13,16,20,27,30,31]. It is expected that as the pulse duration is increased, the melt duration would be increased accordingly. This is supposed to improve the recrystallization process, with a regrown layer having lower density of defects once it has solidified [32], as seen in previous works [1,33]. The additional advantage of this laser set up is its wider laser spot (referred to as "full die" exposure), as compared to other available lasers, avoiding the use of "stitching" patterns to cover bigger areas, as some authors observed that laser stitching patterns increases the dark current of laser annealed devices [4].

3. Experimental

300 mm diameter, p type monocrystalline Si wafers were used as starting material, with a boron concentration of 4×10^{15} cm^{-3} and <100> crystal orientation. Ti ions were ion implanted at an energy of 10 keV in an IMC 200P ion implanter, located at Ion Beam Services (IBS) facilities. The manufacturer assured a relative uniformity better than 2 %, within the implanted area around 185 mm diameter, almost wafer centered. We chose a 7° tilt angle to minimize channeling. Ti dose was set to 3×10^{15} cm^{-2}, high enough to overcome the insulator-to-metal transition or Mott limit so that an impurity band could be formed, as previously verified by simulations using the Stopping and Range of Ions in Matter (SRIM). Low energy ions were chosen in order to get a profile as shallow as possible, aiming to reduce the minimum laser energy required to melt beyond the deepest Ti atoms, expecting to minimize all the damage produced by the ion implantation process.

Samples described above are compared to a second set of wafers, which were fabricated using different ion implantation conditions: a double ion implantation process with a total dose 2×10^{16} cm^{-2}. First, 20 % of total dose is implanted at 35 keV, followed by a second implantation process at 80 %

of total dose and 150 keV of energy, aiming to produce a thick Ti supersaturated layer with a more constant profile, as compared to single ion implantation. 50.8 mm p-type c-Si (<100>) substrates were chosen, with resistivities in the range 1-10 Ω cm, corresponding to boron concentrations between 2×10^{15} cm^{-3} and 2×10^{16} cm^{-3}.

Laser annealing was performed in both sets of wafers using a SCREEN-LASSE LT3100 equipment, located at CEA-LETI facilities. This platform features a 308 nm wavelength XeCl laser source, with a pulse duration at Full Width Half-Maximum (FWHM) of 147 ± 3 ns and an exposed area of 15 x 15 mm^2. In this manuscript, a die is defined as each area that was exposed to the laser process. Relative laser uniformity is assured to be better than 2.5 %. Two different types of wafers were processed with this laser equipment: one non-implanted wafer (used as reference) and a second Ti implanted, with the previously described parameters corresponding to single implantation at 10 keV. Each wafer contained 76 different dies; each die being processed with a different laser condition. Separation between dies was set to 3 mm. Dies were fabricated in two groups of 38. The first group received only one shot at an increasing laser fluence, starting from 0.80 up to 3.60 J cm^{-2}, with steps of 75 mJ cm^{-2}. The second group was fabricated firing two laser shots on each die. The first shot followed the same sequence as in the first group, sweeping from 0.80 to 3.60 J cm^{-2}. The second laser shot was fired for all 38 dies at a fixed value of 2.40 J cm^{-2}. The aim of the second shot was to check the behavior of the supersaturated material after the first one.

Time-Resolved Reflectometry measurements, with a time resolution of 2 ns, were carried out during the NLA process. A laser probe source with a wavelength of 635 nm has been used to measure the reflectivity of the sample during the melting and solidification process caused by the main UV laser. The variations of the reflectivity value over time provide valuable information about the melting status of the surface under study. The TRR experimental set-up is the standard equipment supplied within the SCREEN-LASSE LT3100. More details can be found elsewhere [34].

Haze measurements were performed after the solidification of the material, using a KLA-Tencor Surfscan SP2 equipment, available at CEA-LETI facilities. Haze measurements are mainly used in the industry to monitor the presence of particles on the wafer surface [35] and control the surface roughness [36]. Other authors found a correlation between polycrystalline formation close to the surface and an increase on the Haze value [2]. Haze is expressed in parts per million (ppm) and the higher the value, the higher the deviation from a perfectly reflecting surface. It is determined by impinging a 355 nm wavelength laser spot in glancing angle (set up to 70°) onto the surface under study, which collects information from within the first 30 nm of the wafer surface. The laser is swept across the whole wafer while the latter is rotating at high speed. Extended description of the measurement technique can be found in the literature [35,37,38]. A built-in software processes the data and shows a Haze map of the whole wafer. Five points within each die were measured, and the average is presented in this study, using the standard deviation as the uncertainty.

Ti concentration profiles were obtained using a Dynamic Secondary Ion Mass Spectroscopy (D-SIMS) CAMECA IMS Wf equipment located in STMicroelectronics facilities. Profiles were obtained using a dual beam configuration, being oxygen the element chosen to sputter the surface at an energy of 3 keV. All Ti profiles have been normalized to the silicon signal to avoid any non-uniformity in extraction efficiency during the sputtering process.

For electrical characterization, we used a four-probe sheet resistance AITCO CMT-SR2000N instrument located at Universidad Complutense de Madrid (UCM). The probing point had a separation of 1.014 mm, and the injected current was set from 100 nA to 10 μA depending on the sample under study. Five measurements in different points of the laser exposed surface were taken, avoiding the die borders to minimize the influence of the neighboring dies. The values presented later are the average value for each sample, along with the standard deviation as the uncertainty of the measurement.

Surface roughness was determined by means of Atomic Force Microscopy (AFM) in tapping mode. 5x5 μm scans have been used to extract the RMS values. The equipment used was a Nanoscope multimode IIIA manufactured by Bruker, located at Centro Nacional de Microscopía Electrónica (CNME) facilities in Madrid.

TEM lamellas have been prepared using a Focused Ion Beam Scanning Electron Microscope (FIB-SEM) tool manufactured by Helios, model Nanolab 650 Dual Beam, located at Laboratorio de Microscopía Avanzada (LMA) at Universidad de Zaragoza facilities. After the preparation, cross-section High Resolution Transmission Electron Microscopy (HRTEM) micrographs were obtained using a JEOL 3000F model, also located at CNME, which also features an INCA Energy Dispersive Spectroscopy (EDS) module for qualitative chemical identification of the lamellas. The EDS module was used in Scanning Transmission Electron Microscope (STEM) mode to probe locally the Ti implanted layers. EDS parameter were set to 1,250,000x magnification and 200 keV of acceleration.

4. Results

TRR results are shown first in **Figure 1**. Only four representative curves are displayed for clarity, coming from samples that were laser annealed only once. The analysis, however, included all 38 different laser conditions. More information can be found in the supplementary material, **Figure S.1**.

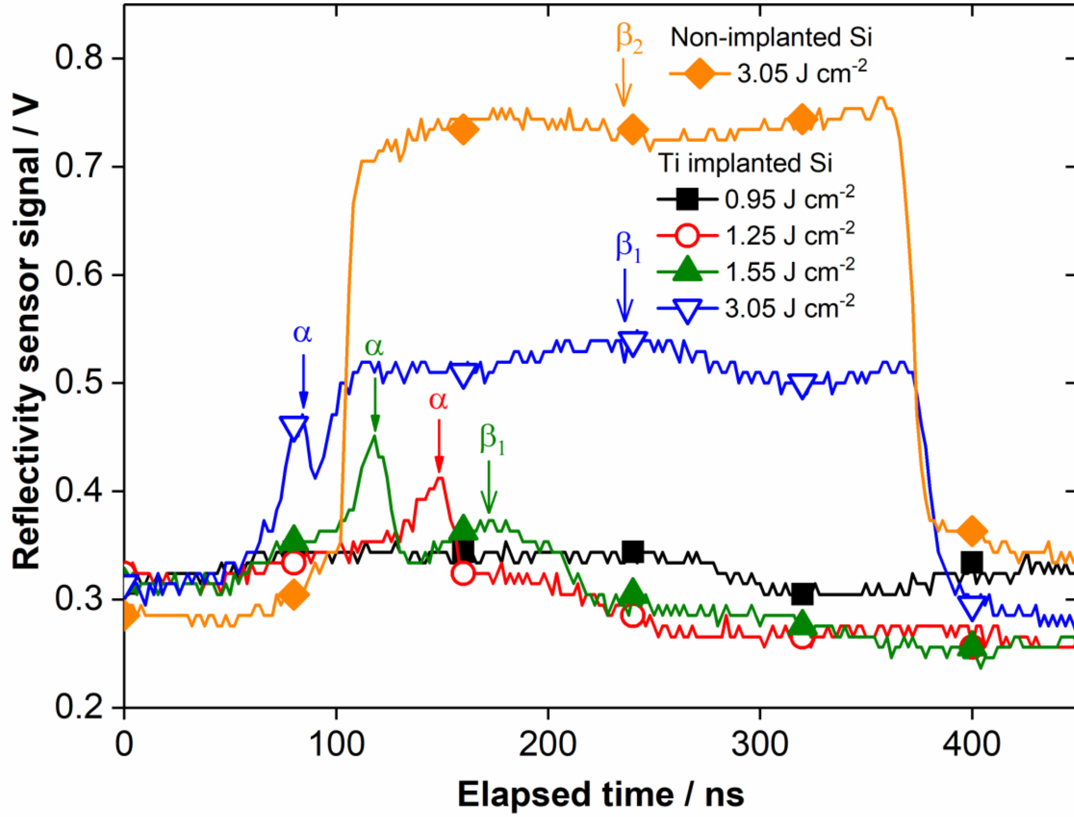

Figure 1. Time Resolved Reflectometry (TRR) measurements for samples implanted at 10 keV with a Ti dose of 3×10^{15} cm^{-2}, subsequently annealed at different pulsed laser energy densities. Each symbol in the legend corresponds to a laser fluence of: ■ 0.95 J cm^{-2}, ○ 1.25 J cm^{-2}, Δ 1.55 J cm^{-2} and ∇ 3.05 J cm^{-2}, the four of them for Ti implanted samples. The last curve represents the non-implanted sample by ◊ at a fluence of 3.05 J cm^{-2}. Left Y-axis represents the voltage measured by the sensor. Arrows in the Figure indicate the important peaks and plateaus mentioned in the text.

Four different behaviors were found while examining TRR curves. Starting from 0.80 to 1.10 J cm^{-2}, TRR profiles did not display any significant feature, as shown in the representative curve at 0.95 J cm^{-2}. A similar behavior was found for non-implanted Si samples annealed using the same fluence interval.

Increasing the laser fluence beyond 1.10 J cm^{-2} led to changes in the TRR curves, which display an asymmetric peak around 140 ns from trigger, labelled as α in **Figure 1**. The α peak appears at shorter times, displaying also higher reflectivity values, as the laser fluence increases. Up to 1.40 J cm^{-2} this is the only peak observed. Non-implanted samples did not show any observable feature in the same interval.

The third regime starts at 1.40 J cm^{-2} and extends up to 1.93 J cm^{-2}. Its main characteristic is the emergence of a second peak, after the α peak, labelled as β_1, for times around 170 ns from the origin. This peak follows a similar trend as the α peak. The peak emerges earlier when laser fluence is increased, and the maximum reflectivity value at the peak is higher as well. β_1 peak, however, does increase its width along with laser fluence, as opposed to α_1 peak (see **Figure 2**). In this regime, at 1.85 J cm^{-2}, non-implanted dies showed a peak, labelled as the β_2 peak (see **Figure S.1** in the supplementary material).

At the highest energy regime, for laser fluences higher than 1.70 J cm^{-2}, the β_1 feature transitions from a peak to a plateau at around 1.93 J cm^{-2}. The reflectance saturates at around 0.5 V in all TRR curves measured from 2.00 J cm^{-2} to 3.58 J cm^{-2}, a value consistently higher than the reflectance of the α peak. Non-implanted c-Si samples show an even higher saturation voltage on the β_2 plateau, around 0.73 V. For both implanted and bare Si samples, the plateau duration increases along with the laser fluence, in a linear-like dependence, as shown in **Figure 2**. There are differences between β_1 (Ti implanted samples) and β_2 (non-implanted Si samples) features though. More laser energy was required for the β_2 peak to appear, at 1.85 J cm^{-2}, compared to 1.40 J cm^{-2} in case of β_1 peak.

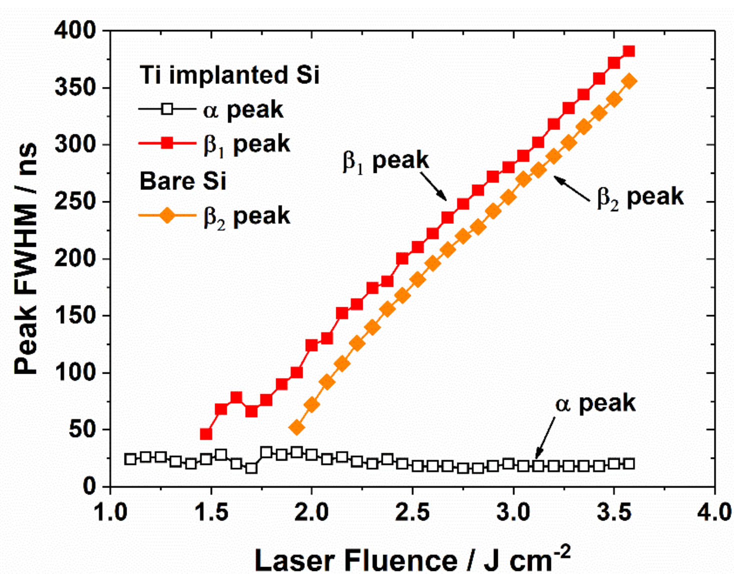

Figure 2. Peak Full Width at Half Maximum of α and β_1 peaks of Ti implanted samples and β_2 peaks of non-implanted Si samples, as a function of the laser fluence.

Surface morphology is characterized using two different techniques, HM and AFM. AFM roughness RMS value was obtained from 5x5 µm scans, some of them shown in **Figure S.4** of the supplementary material. Haze, AFM and sheet resistance measurements were performed after the solidification of the material. Results for the three techniques are shown in **Figure 3**.

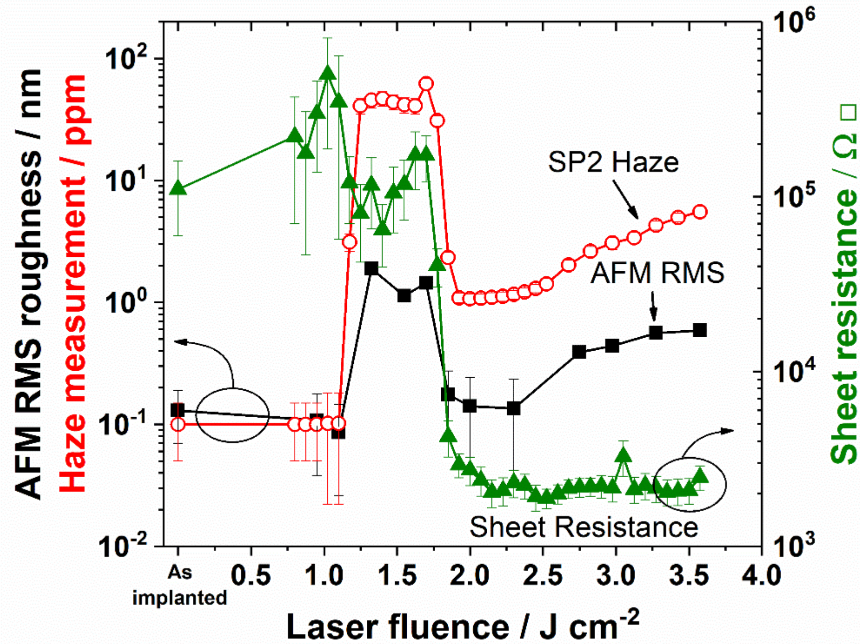

Figure 3. Surface and electrical characterization of Ti implanted samples as a function of the laser energy density. For all curves, a laser energy density of 0 J cm^{-2} represents the "as-implanted" sample. AFM RMS roughness (■) in nanometers and Haze values (○), in parts per million, corresponds to the left Y-axis on logarithmic scale. On the right Y-axis, also on logarithmic scale, sheet resistance is shown (Δ). Standard deviation is used as the uncertainty of the measurements.

Three distinguishable regimes were found within the same fluence values for the three different techniques. The first regime comprises from the as-implanted sample (non-laser annealed) up to 1.10 J cm^{-2}. Haze values (red circles), remain constant, in the order of 0.1 ppm. AFM RMS roughness (black squares) values are low, slightly above the minimum resolution of the AFM microscope, leading to high relative uncertainties. Sheet resistance (green triangles), in the order of tens of kΩ □, also remains flat.

In the second regime, from 1.10 J cm^{-2} up to 1.85 J cm^{-2}, haze increases abruptly up to around 40 ppm, trend that is also seen in the RMS roughness, where 2 nm RMS roughness values are measured. On the contrary, sheet resistance slightly decreases to around 100 kΩ □, but the uncertainty is high.

The third regime extends beyond 1.85 J cm^{-2}. Haze drops down significantly, yet values are higher than in the first regime, monotonically increasing along with laser fluence. A similar trend is observed for AFM RMS roughness values. Finally, sheet resistance sees a substantial drop, down to around 2 kΩ □, where it remains flat.

There is a clear correlation between the Haze and the AFM RMS roughness value, as previously reported by other authors [2]. Judging from the available experimental data and their related uncertainties, Haze measurements may be more sensible to slight variations, as compared to AFM RMS value.

High Resolution cross-sectional TEM micrographs were obtained to check the crystalline quality of the samples, which are shown hereafter in **Figure 4**.

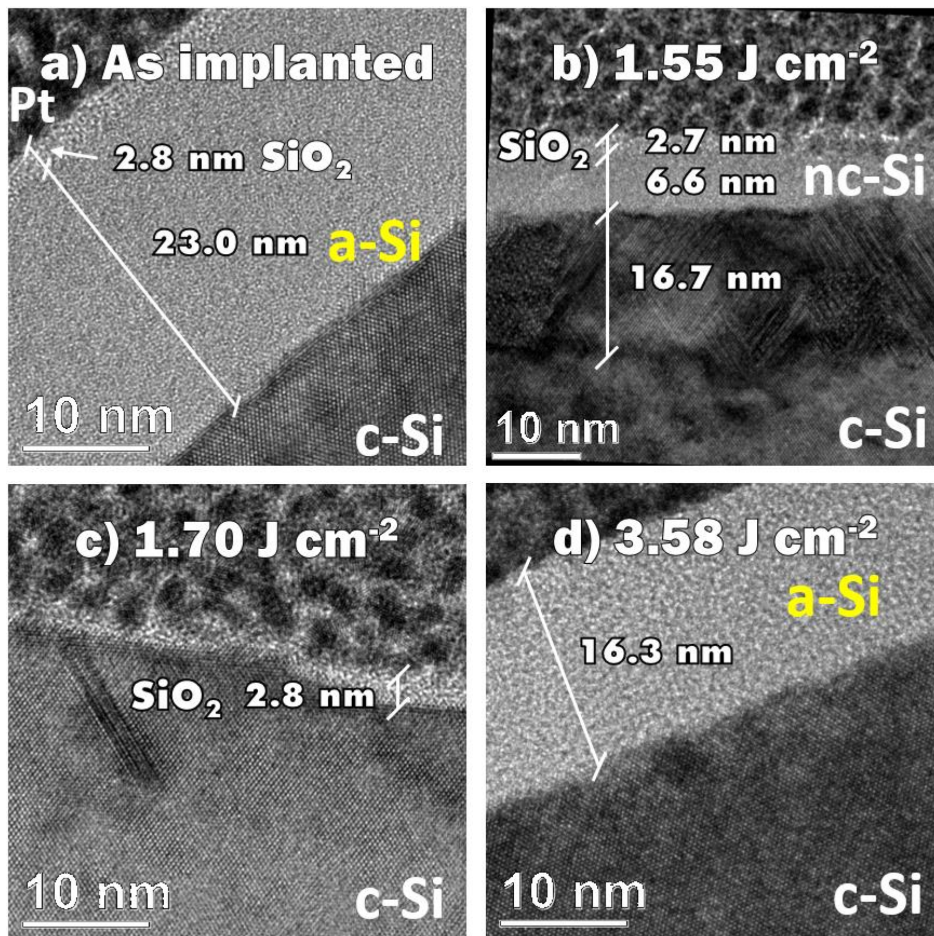

Figure 4. Cross-sectional HRTEM micrographs for several laser energy densities used to melt Ti implanted Si samples. From a) to d): as-implanted (no laser annealing), 1.55 J cm^{-2}, 1.70 J cm^{-2} and 3.58 J cm^{-2}.

Considering **Figure 4** and **Figure S.3** from the supplementary material, the same three different regimes already identified in previous lines from **Figure 3** were found. **Figure 4a** shows the HRTEM of the as-implanted sample, where an amorphized layer of 23 nm is found under a 2.8 nm native SiO_2 layer, as identified by means of EDS technique. The sample annealed at 0.95 J cm^{-2} was very similar to the as implanted one, having the same two layers (oxide + a-Si) with the same thicknesses (see **Figure S.3** of the supplementary material). Within the second regime, up to three different layers were found: a first amorphous layer of 2.8 nm thickness, identified as the native oxide; a second nanocrystalline layer, containing some randomly oriented nanocrystals; and a third layer consisting of polycrystalline or defective monocrystalline silicon. The sum of the thicknesses of the last two layers was equal to 23 nm for all inspected samples, the same value as the amorphous layer from the as-implanted sample. **Figure 4b** represents this behavior (laser fluence of 1.55 J cm^{-2}) where the polycrystalline layer is up to 17 nm thick, and a surficial nanocrystalline layer 5 nm thick. In this second regime, the thickness of the polycrystalline layer increased along with laser fluence, at the expense of the surficial a-Si thickness, which reduced at the same rate. This stack of layers is not homogenous, as there are other areas where only nanocrystals were observed, without any trace of larger polycristals underneath.

The third regime starts at laser fluences higher than 1.85 J cm^{-2}. HRTEM micrographs in this regime show a single amorphous-like layer whose thickness increases along with the laser fluence. For the sample annealed at 2.00 J cm^{-2} (shown on **Figure S.5** of the supplementary material), the abovementioned amorphous layer is around 7 nm thick. EDS measurements showed that the first 2.8 nm are due to the presence of oxygen, while the rest of the layer is composed of silicon, being around 3.5-4.5 nm thick. Similar a-Si layers are observed for 2.75 and 3.58 J cm^{-2} with 5.3 nm and 17 nm of thickness respectively. The latter is shown in **Figure 4d**.

Finally, SIMS measurements are included in **Figure 5** to verify that the necessary amount of Ti has been introduced into the Si lattice, high enough to overcome the supersaturating or Mott limit.

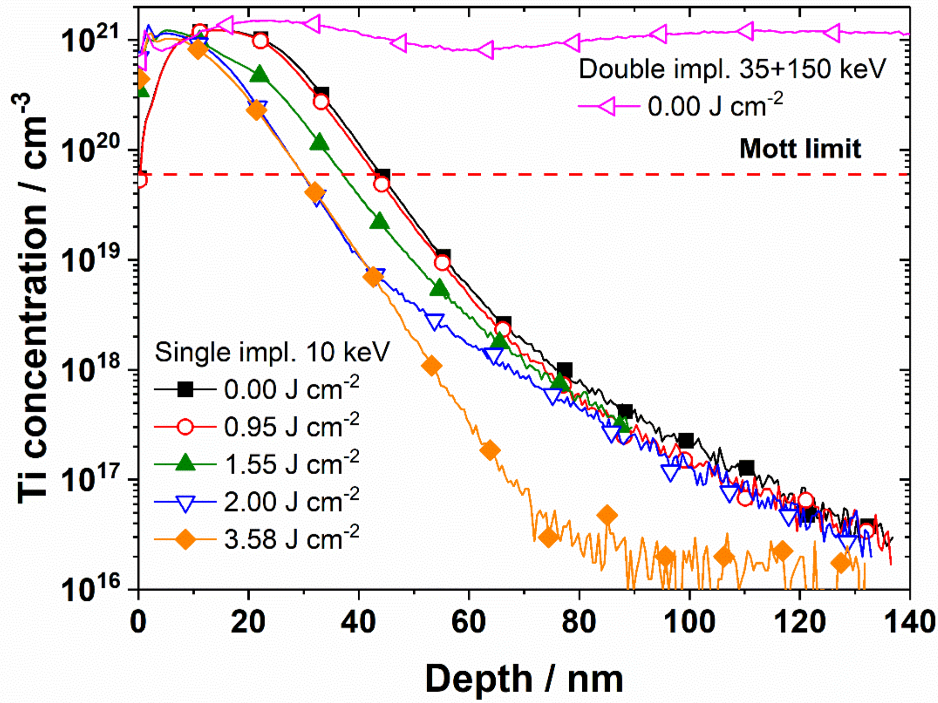

Figure 5. D-SIMS depth profile on logarithmic scale for several Ti implanted samples subsequently laser annealed at various fluences. Horizontal dashed red line represents the supersaturating (Mott) limit. Different samples with increasing laser fluence are represented by: (■) as-implanted reference, (○) 0.95 J cm^{-2}, (Δ) 1.55 J cm^{-2} and (∇) 2.00 J cm^{-2}, (◊) 3.58 J cm^{-2}. The previous samples were implanted using a single step, with an energy of 10 keV and Ti dose of 3×10^{15} cm^{-2}. Finally, (◅) stand for the as-implanted sample having a double ion implantation process at a total dose of 2×10^{16} cm^{-2} and an energy of 35 keV for the first ion implantation step and 150 keV for the second, shown for comparison.

The aim of the ion implantation process is to obtain Ti supersaturated layers, requiring Ti concentrations in the order of 6×10^{19}-10^{20} cm^{-3} (the former as theoretically obtained by other authors [39] and the latter as experimentally measured in other works [40]). All laser annealed samples achieved sufficient concentration to attain supersaturation.

5. Discussion

In this manuscript, industry-relevant Time-Resolved Reflectometry and Haze measurements techniques are applied to investigate the recrystallization process during Nanosecond Laser Annealing on Ti supersaturated Si substrates, which are then compared to more conventional approaches, like HRTEM, AFM, D-SIMS and sheet resistance techniques. All the techniques point towards at least three different regimes where the Ti implanted, laser-annealed samples behave differently.

The Ti dose used to supersaturate the silicon substrate is high enough to produce an amorphized surficial layer 23 nm thick, as it has been confirmed by HRTEM micrographs from **Figure 4a**. Therefore, the melting process of the samples described in this manuscript may be severely influenced by the presence of this amorphized layer, in contrast to the bare Si samples with no Ti implantation, where only a monocrystalline phase is present. This is reflected in the fact that three or four different recrystallization regimes (depending on the technique) are observed when laser-annealing Ti supersaturated Si samples, while only two regimes are observed in the case of pristine Si.

Before entering further discussion regarding Ti supersaturated Si samples, a brief introduction of amorphous silicon melting processes, compared to poly- or monocrystalline substrates can be found below.

According to several works, it is commonly accepted that amorphous silicon has a lower melting point, around 225 ± 50 K lower than crystalline silicon [41], commonly accepted to be 1683 K [32]. Thus, it is expected that the a-Si layer will melt at lower energies than the c-Si layer, as less energy is needed to reach its melting point. Amorphous silicon has an absorption coefficient at λ=308 nm, the wavelength of the UV laser used in this study, close to that of crystalline silicon, as it has been pointed out in other works [42,43]. Thus, the amount of energy absorbed by either amorphous or crystalline silicon is expected to be similar, and differences in the minimum laser fluence needed to melt the layers may be attributed mostly to the difference in the melting temperature.

There are several references in the literature [44,45] describing the melting and subsequent solidifying processes of amorphous silicon layers, usually referred to as “explosive recrystallization”. When an amorphous Si layer receives a certain amount of energy, it may start to melt, solidifying shortly after as polycrystalline or monocrystalline phase, as they are energetically more favorable phases [46]. However, if the solidification front speed is not sufficiently low (some references set the limit at 15 m s^{-1}) [47], the recrystallization process could result again in an amorphously regrown layer.

The transition from amorphous to poly- or monocrystalline phase is a transition of first order [41], which implies a latent heat of fusion that is released to the surroundings, mainly the underlying substrate. The released energy may be absorbed first by the amorphous layer beneath the originally melted layer. This heat is enough to melt again the remaining amorphous silicon, thus propagating a melting front that moves towards the substrate until the still-defective crystalline phase is encountered [45]. There is a range in which the amorphous layer may be fully melted, but there is still not enough energy to melt the crystalline phase as there is a difference of more than 200 K between their melting points. If the laser energy is increased furthermore, at some point there may be enough energy to melt part of the first c-Si atomic layers. Then, at this point, the recrystallization process is expected to produce a monocrystalline structure, ideally free of defects.

Main discussion

It is well documented that silicon surface reflectivity increases along with the surface temperature [48]. TRR technique relies on this physical principle to probe the melting and solidifications processes during the NLA process [49]. Upon the onset of melting, silicon reflectivity reaches a saturation value, which quickly decays as soon as the material solidifies. Then, the width of the TRR plateau can be used to determine the duration of the melting process.

Ti supersaturated samples exhibited two different peaks. Thus, a two-phase melting process could be inferred, one involving the α peak and the second involving the β_1 peak plateau. On the other side, only one melting process was found for bare Si substrates, associated with the β_2 peak plateau. How these peaks evolve as the laser fluence is increased, as well as other material properties described by the rest of the techniques, were used to define the four different recrystallization regimes described below, applicable for Ti supersaturated Si samples.

a) ***Sub-melt*** *regime. Laser fluences from 0.00 up to 1.10 J cm*$^{-2}$.

The laser fluence is too low to even start melting the amorphized layer. TRR signal is relatively flat, with no visible features. HRTEM micrographs show no change in terms of crystal quality on the

amorphized layer. D-SIMS Ti concentration profile does not show any Ti redistribution, consistent with the poor Ti diffusion coefficient in solid Si, considering that the heating process happens in the nanosecond scale. Haze values and AFM RMS roughness are close to those of the as-implanted layer. A slight increase in the sheet resistance can be seen, although the uncertainty of the measurement in this regime is rather high and differences could be considered as part of the uncertainty.

Non-implanted silicon samples did not exhibit any peak on TRR curves.

b) ***First melt and solidification*** *regime. Laser fluences from 1.10 up to 1.40 J cm^{-2}.*

The energy provided by the laser is high enough to start melting part of the amorphized surface, but not high enough to melt the crystalline part. This first melt is reflected on TRR curves as the α peak. The melting process is brief, in the order of 25 ns, with no direct influence of the laser fluence on the melt duration (see **Figure 2**). Both properties are consistent with the explosive recrystallization process of an amorphized layer atop of a crystalline substrate, as previously discussed. The brief duration of the α peak is in line with the rapid cooling as it is an undercooled molten phase, which may rapidly solidify as nano- or polycrystalline. The molten thickness should remain constant, as only the amorphized layer could be melted in this regime, which would explain why the duration of the melting process is almost constant. The absence of this peak in the non-implanted Si samples also confirms our hypothesis, as the substrate was already crystalline before the laser process.

As the molten amorphous layer recrystallizes, it might solidify as nano- or polycrystalline structures, as it is more energetically favorable. These nanocrystalline structures are captured by HRTEM micrographs, see **Figure S.5** in the supplementary material. Haze values increase by more than a factor of 20, following AFM RMS roughness measurements the same trend, which is consistent with the nano- or polycrystals pushing the surface and thus increasing the surface roughness.

Average sheet resistance values seem to decrease, but again, the uncertainty in this regime is rather high and it is hard to extract more conclusions, apart from the fact that the values are consistently high.

Non-implanted silicon samples did not exhibit any peak on TRR curves.

c) ***Second melt and crystallization onset*** *regime. Laser fluences from 1.40 up to 1.85 J cm^{-2}.*

The laser keeps putting energy into the sample, compared to the previous regime, which is absorbed first by the freshly formed nanocrystals coming from the explosive recrystallization. TRR curves coming from samples belonging to this regime show the formation of a second peak, the β_1 peak, which shows higher reflectance than the α peak. This is consistent with a higher temperature melting process, associated with a somewhat ordered silicon structure, like nano-, poly- or monocrystal melting process, as discussed before. The reflectance has not saturated yet, which implies that the temperature is still not high enough to fully melt monocrystalline silicon. However, defects coming from the ion implantation process may decrease the melting temperature compared to perfect monocrystalline structures, as described by other authors [50], which means that there is a range between the fusion point of amorphous silicon and the fusion point of monocrystalline silicon where nano- or polycrystalline structures could still melt forming a less undercooled liquid phase.

Following the trend of the β_1 peak on TRR curves from this regime, an increase in the peak width is observed as laser energy increases, in contrast to the behavior of the α peak (see **Figure 2**). As the temperature on the melted layer approaches the melting temperature of monocrystalline silicon, the surface takes longer to cool, which provides more time for the atoms to reorganize in more stable structures. Therefore, after the solidification following this second melt event, the average size of the nanocrystals is expected to increase. This is supported by HRTEM micrographs, see **Figure 4b** and **Figure 4c**. As described in the results section, the thickness of the polycrystalline layer increases along with the laser fluence, at the expense of the surficial nanocrystalline layer, which shrinks down at the same rate. The extreme case happens at 1.70 J cm^{-2} (**Figure 4c**), where no nanocrystalline layer was identified, aside from the native oxide.

Haze and AFM RMS roughness keep the same trend as in the previous regime. For both techniques, there is no measurable distinction between the first melt and second melt regimes. The same behavior

is found on sheet resistance measurements, there is no measurable change compared to the previous regime; values are high, consistent with a poorly crystallized structure.

Non-implanted silicon samples did not exhibit any peak on TRR curves.

*d) **High energy** regime. Laser fluences higher than 1.85 J cm-2.*

The laser energy is high enough to melt past the original amorphous-crystalline interface coming from the ion implantation process, and the temperature on the sample is high enough to melt monocrystalline silicon. In this regime, the reflectance value of Ti supersaturated samples saturates at around 0.5 V, and thus the β_1 peak evolves into a plateau.

In this regime, TRR curves from non-implanted Si show significant changes. At 1.85 J cm^{-2} a peak appears, labelled as β_2 peak (**Figure 2**), that becomes into a plateau at 2.00 J cm^{-2}, with a much higher saturation value than Ti supersaturated samples, at 0.72 V. This small difference of around 0.2 J cm^{-2} between the minimum laser fluence needed to see β_1 and β_2 plateaus could be explained by the amount of damage that is still present in the crystalline phase under the amorphous implanted layer. Although the phase is crystalline, some defects are expected closer to the amorphous-crystalline interface (the so-called "end of range" defects [50]). The induced damage by the ion implantation could lower the threshold value necessary to melt the layer.

The reflectivity saturation value of β_1 plateaus is much lower than for β_2 plateaus, which may indicate a different light absorption process on Ti implanted samples, as compared to bulk Si samples at λ=635 nm during the melted phase. Other works measured the refractive index, (although in the solid phase, at room temperature) of Ti implanted samples [27], which is close to that of bare Si. If we assume that the real part of the refractive index does not change substantially after the ion implantation of Ti atoms, then the difference in the reflectivity could be explained by a higher absorption process on Ti implanted samples. More evidence is needed to shed more light on the origin of the reduced reflectivity shown on Ti implanted samples.

Figure 2 shows the peak FWHM as a function of the laser fluence of both β_1 and β_2 peaks, which exhibit a linear behavior with respect to the laser fluence. The case of non-implanted Si has been already described elsewhere as linear [51]. The present manuscript reports that Ti supersaturated Si also shows a linear behavior, closely following that of non-implanted Si. However, this may not be the case for silicon supersaturated with other elements, as for example As, reported elsewhere [52]. Although β_1 and β_2 peaks have been linked to the same melting process of crystalline Si, Ti implanted samples remained in the liquid phase on average 20 ± 5 ns longer than non-implanted Si. Other authors pointed out that the thermal conductivity of heavily implanted layers could be lowered due phonon scattering processes induced by the presence of impurities, vacancies or stacking faults [53]. Therefore, lower thermal conductivity of heavily damaged (supersaturated) Si could result in longer melting times, as experimentally measured. Optical properties of the implanted layer may also play a role: the absorption coefficient of Ti implanted samples could be higher than the non-implanted samples, which would imply that more energy could be absorbed, resulting in longer melting times. A third possibility is proposed: since damaged silicon melts at lower temperatures, a lower fraction of the total energy absorbed by the material would be used to melt the implanted layer. Then, more energy is available to increase the temperature of the molten phase, resulting in longer cooling times. The three possibilities are non-excluding and could be happening at the same time.

Surface roughness decreases abruptly in the high energy regime, as seen in both Haze and AFM measurements, which is consistent with the absence of polycrystals in this regime, as evidenced by HRTEM (**Figure 4c** and **4d**). Still, roughness values are higher than in the sub-melt regime. For energy densities well above 2.50 J cm^{-2}, surface roughness and Haze results both show a new trend towards higher values. It is well known that after a NLA process some roughness may be induced on the surface [54]. This phenomenon is used, for example, to produce black silicon [55–57]. The average feature size of the induced roughness is small compared to those of black silicon, with average height of 2-3 nm and width of tens of nanometers, but noticeable enough to be detected by either Haze or AFM measurements.

Sheet resistance measurements drastically drop too in the high energy regime, which points out to a good recrystallization process with fewer defects than in lower energy regimes. However, the sheet resistance value is not matching that of a conduction in parallel of the substrate and the Ti supersaturated layer. The value is two orders of magnitude higher than the expected sheet resistance of the substrate alone, which points out to a decoupling process between the Ti implanted layer and the substrate, as it has been measured in other works [58,59]. This would imply an electrical barrier between the Ti supersaturated layer and the substrate. Current could be blocked in one direction, like in a PN junction, thus measuring only the sheet resistance associated to the supersaturated layer.

In the high energy regime, all damage coming from the ion implantation is expected to be annealed since the laser fluence is high enough to melt past the original amorphous-crystalline interface, so that the solidification front may take a crystalline seed to regrow from.

However, upon inspection of the HRTEM micrographs, an amorphous layer was again present, becoming thicker as the laser fluence is increased (see surficial layer on Figure 4d). This is the case for samples with laser fluences higher than 2.0 J cm^{-2}. The thickness of this unexpected amorphous layer is thinner than the original amorphized layer, which points out to a partial recrystallization process, that somehow became amorphous in the latest stages of solidification. It is the first time that a regrown amorphous layer is reported for Si supersaturated samples subsequently annealed using a nanosecond laser. Other works have documented it but with different laser processes, namely femtosecond laser annealing, and with other chemical species such as S, Se or Te [55,60].

Multiple options have been considered to explain the origin of the regrown amorphous layer. Presence of oxygen in the film as a possible source was discarded as no oxygen was detected in the layer, aside from the native oxide. A second hypothesis considered there may be an excessive accumulation of Ti atoms close to the surface, possibly forming silicides or agglomerates. However, when using EDS on STEM mode, Ti atoms were not consistently detected on all samples, only on the sample annealed at 2.0 J cm^{-2}, which showed a relative Ti concentration lower than 2 %, very close to the EDS detection

limit, and much lower than the Ti concentration required to form TiSi, where other authors reported around 45 % of Ti concentration [61].

Even with no visible silicidation, Ti concentration could still be too high to allow for a proper recrystallization process. However, samples with nine times higher dose, but with higher ion implantation energy (2” samples, described in the experimental section), never showed any amorphous layer close to the surface. D-SIMS profile of the latter sample (**Figure 5**) shows that Ti concentration stays well above that of the samples with single implantation and a dose of 3×10^{15} cm^{-2}, while still keeping a monocrystalline structure (see HRTEM in **Figure S.7** from the supplementary material).

The most plausible explanation for this anomalous amorphous layer is that the recrystallization speed could become higher as the solidifying front approaches the surface, beyond the critical value of 15 m s^{-1} [47], resulting in an amorphously regrown layer. Again, this was never observed before on samples annealed with the same laser process, but with higher ion implantation energy. As the ion implantation energy is low in the samples on this manuscript (10 keV), all Ti atoms are confined in a thinner layer than when using higher ion implantation energies. The energy of implantation plays a key role in the thickness of the amorphized layer after the ion implantation process; higher energies may lead to thicker amorphized layers. During the first moments of energy absorption, most energy is trapped in the amorphized layer. That would imply that higher temperatures would be expected in thinner layers. Since the speed of recrystallization depends on the gradient of the temperature, it is expected that, if the temperature is higher, the solidification speed would be also higher [62]. This possibility is consistent with what we observed from available data in the high energy regime: the thickness of the regrown amorphous layer is increasing along with the laser fluence. Also, other references already stated that excimer laser melting thin amorphous films could be more challenging as compared to thicker films due to non-irregularities in the light absorption and subsequent melting processes [63]. As a possible solution to mitigate the presence of this undesired amorphous layer, the authors propose to increase the ion implantation energy.

As a final experiment to further understand the meaning of α and β peaks, Ti supersaturated layers were submitted to two different NLA processes on the same area, (see TRR curves on **Figure S.3** in supplementary material). If during the first laser shot the α peak was present (so the amorphized layer was melted, at fluences higher than 1.10 J cm^{-2}), then during the second shot only the β_1 peak would be observable. However, if the first laser shot had a fluence lower than 1.10 J cm^{-2} (neither α nor β_1 appeared), then both peaks would appear only on the second shot. In other words, the α peak appeared only once when doing several laser shots on Ti implanted samples. This fact points out again to the nature of the amorphous layer, that becomes nanocrystalline or monocrystalline (depending on the laser fluence) after it was melted by effect of the laser.

Relative to crystal quality of supersaturated layers, several works state that it is very difficult to achieve Ti supersaturation on Si without "cellular breakdown" phenomenon, in which columnar Ti-rich structures appear clearly visible on HRTEM micrographs [64,65]. The samples studied in this manuscript, having a Ti dose of 3×10^{15} cm^{-2}, confirms that it is possible to achieve Si supersaturation with Ti atoms without necessarily exhibiting the cellular breakdown behavior.

6. Conclusions

This manuscript describes the different recrystallization regimes of Ti supersaturated layers during an UV nanosecond annealing process, identified by means of Time Resolve Reflectometry and Haze measurements. Both techniques are fast, non-invasive and performed at 300 mm full wafer level, making them ideal technologies to characterize supersaturated materials targeting high volume manufacturing environments.

Time Resolved Reflectometry has been used to detect two different reflectance peaks, involving two different melting processes. The α peak has been linked to low temperature, amorphous Si melting processes. β peaks describe the melting process of ordered Si structures, as nano-, poly- or monocrystalline Si phases, which require higher melting temperatures than amorphous Si. Four different recrystallization regimes have been defined based on the behavior of both peaks. In the sub-

melt regime, below 1.10 J cm^{-2}, the laser fluence is not high enough to kickstart the melting process of the amorphized layer. In the first melt and crystallization regime, between 1.10 and 1.40 J cm^{-2}, the laser fluence is able to only melt the amorphized layer. During the second melt and onset of crystallization regime, between 1.40 and 1.85 J cm^{-2}, the laser energy is high enough to melt the newly solidified nano- or polycrystalline structure that resulted from the first melt regime, but not high enough to melt pristine, monocrystalline Si. In the high energy regime, above 1.85 J cm^{-2}, the laser has enough energy to melt monocrystalline Si, past the original amorphous-crystalline interface. The implanted layer is mostly monocrystalline, with no visible defects. However, an unexpected amorphous layer is found for laser fluences higher than 2.00 J cm^{-2}. It has been proposed that the solidification speed becomes too fast to allow for a proper recrystallization, resulting in the surficial amorphous layers. Haze measurements have been used to detect polycrystalline phases during the first and second recrystallization regimes. More common techniques, such as AFM and HRTEM, were used to confirm the hypotheses. Given the results, haze is much more sensitive to surface changes than AFM measurements, while being much faster and easily performed at wafer level.

Two key signatures have been linked to a good recrystallization process on Ti supersaturated Si: a) a sudden Haze drop after a zone of maximum Haze and b) the reflectivity saturation of the β_1 peak found in TRR measurements. The total amount of time and resources spent in these two measurements is reduced as compared to more conventional techniques, such as AFM or HRTEM.

Supporting Information

Supporting Information is available from the editor or from the author.

Acknowledgements

The Thin Films and Microelectronics group acknowledges the “CAI Técnicas Físicas”. Special thanks to Rosa Cimas and Pablo Fernández. D. Montero would also like to thank K. Dabertrand, S. Chhun, T. Dalleau and B. Rodrigues.

The Thin Films and Microelectronics group acknowledges the Spanish Ministry of Science and Culture for their financial support via two main research projects: TEC2013-41730-R and TEC2017-

84378-R. The contribution coming from the project Madrid-PV (project code S2013 MAE-2780) granted by the Comunidad de Madrid is also acknowledged.

D. Montero would like to acknowledge an FPI grant number BES-2014-067585 coming from the Spanish Ministry of Economics and Competitiveness and the “Ayudas a la movilidad predoctoral”, grant provided by the same organism with grant code EEBB-I-17-12315.

Received: ((will be filled in by the editorial staff))
Revised: ((will be filled in by the editorial staff))
Published online: ((will be filled in by the editorial staff))

References

[1] Venturini J, Hernandez M, Kerrien G, Laviron C, Camel D, Santailler J L, Sarnet T and Boulmer J 2004 Excimer laser thermal processing of ultra-shallow junction: laser pulse duration *Thin Solid Films* **453–454** 145–9

[2] Kerdilès S, Alba P A, Mathieu B, Veillerot M, Kachtouli R, Besson P, Denis H, Mazzamuto F, Toqué-Trésonne I, Huet K and Fenouillet-Béranger C 2016 Dopant activation and crystal recovery in arsenic-implanted ultra-thin silicon-on-insulator structures using 308nm nanosecond laser annealing *2016 16th International Workshop on Junction Technology (IWJT)* pp 72–5

[3] Huet K, Mazzamuto F, Tabata T, Toqué-Tresonne I and Mori Y 2017 Doping of semiconductor devices by Laser Thermal Annealing *Mater Sci Semicond Process* **62** 92–102

[4] Huet K, Boniface C, Negru R, Aing P and Venturini J 2010 Full Device Exposure Laser Thermal Annealing: High performance and high yield junction formation process *2010 18th International Conference on Advanced Thermal Processing of Semiconductors (RTP)* (IEEE) pp 50–2

[5] Akane T, Nii T and Matumoto S 1992 Two-Step Doping Using Excimer Laser in Boron Doping of Silicon *Jpn J Appl Phys* **31** 4437–40

[6] Matsumoto S, Yoshioka S, Wada J, Inui S and Uwasawa K 1990 Boron doping of silicon by ArF excimer laser irradiation in B_2H_6 *J Appl Phys* **67** 7204–10

[7] Acosta Alba P, Kerdiles S, Mathieu B, Kachtouli R, Mazzamuto F, Toque-Tresonne I, Huet K, Besson P, Veillerot M, Aussenac F and Fenouillet-Beranger C 2016 Nanosecond Laser Annealing for Phosphorous Activation in Ultra-Thin Implanted Silicon-On-Insulator Substrates *2016 21st International Conference on Ion Implantation Technology (IIT)* (IEEE) pp 1–4

[8] Brotherton S D, McCulloch D J, Clegg J B and Gowers J P 1993 Excimer-laser-annealed poly-Si thin-film transistors *IEEE Trans Electron Devices* **40** 407–13

[9] Carey P G, Sigmon T W, Press R L and Fahlen T S 1985 Ultra-shallow high-concentration boron profiles for CMOS processing *IEEE Electron Device Letters* **6** 291–3

[10] Olea J, Toledano-Luque M, Pastor D, González-Díaz G and Mártil I 2008 Titanium doped silicon layers with very high concentration *J Appl Phys* **104** 016105

[11] Olea J, Pastor D, Toledano-Luque M, San-Andres E, Martil I and Gonzalez-Diaz G 2009 High Quality Ti-Implanted Si Layers Above Solid Solubility Limit *2009 Spanish Conference on Electron Devices* (IEEE) pp 38–41

[12] Olea J, Toledano-Luque M, Pastor D, San-Andrés E, Mártil I and González-Díaz G 2010 High quality Ti-implanted Si layers above the Mott limit *J Appl Phys* **107** 103524

[13] García-Hemme E, García-Hernansanz R, Olea J, Pastor D, del Prado A, Mártil I and Gónzalez-Díaz G 2012 Ion implantation and pulsed laser melting processing for the development of an intermediate band material *AIP Conf Proc* pp 54–7

[14] García-Hemme E, García-Hernansanz R, Olea J, Pastor D, del Prado A, Mártil I and González-Díaz G 2013 Far infrared photoconductivity in a silicon based material: Vanadium supersaturated silicon *Appl Phys Lett* **103** 032101

[15] Garcia-Hemme E, García G, Palacios P, Montero D, García-Hernansanz R, Gonzalez-Diaz G and Wahnon P 2017 Vanadium supersaturated silicon system: a theoretical and experimental approach *J Phys D Appl Phys* **50**

[16] Mailoa J P, Akey A J, Simmons C B, Hutchinson D, Mathews J, Sullivan J T, Recht D, Winkler M T, Williams J S, Warrender J M, Persans P D, Aziz M J and Buonassisi T 2014 Hyperdoped silicon sub-band gap photoresponse for an intermediate band solar cell in silicon *2014 IEEE 40th Photovoltaic Specialist Conference (PVSC)* (IEEE) pp 1073–6

[17] Wang M, Berencén Y, García-Hemme E, Prucnal S, Hübner R, Yuan Y, Xu C, Rebohle L, Böttger R, Heller R, Schneider H, Skorupa W, Helm M and Zhou S 2018 Extended Infrared Photoresponse in Te-Hyperdoped Si at Room Temperature *Phys Rev Appl* **10** 024054

[18] Wang M, Hübner R, Xu C, Xie Y, Berencén Y, Heller R, Rebohle L, Helm M, Prucnal S and Zhou S 2019 Thermal stability of Te-hyperdoped Si: Atomic-scale correlation of the structural, electrical, and optical properties *Phys Rev Mater* **3** 044606

[19] Liu F, Prucnal S, Yuan Y, Heller R, Berencén Y, Böttger R, Rebohle L, Skorupa W, Helm M and Zhou S 2018 Structural and electrical properties of Se-hyperdoped Si via ion implantation and flash lamp annealing *Nucl Instrum Methods Phys Res B* **424** 52–5

[20] Kim T G, Warrender J M and Aziz M J 2006 Strong sub-band-gap infrared absorption in silicon supersaturated with sulfur *Appl Phys Lett* **88** 241902

[21] Ertekin E, Winkler M T, Recht D, Said A J, Aziz M J, Buonassisi T and Grossman J C 2012 Insulator-to-Metal Transition in Selenium-Hyperdoped Silicon: Observation and Origin *Phys Rev Lett* **108** 026401

[22] Yang W, Akey A J, Smillie L A, Mailoa J P, Johnson B C, McCallum J C, Macdonald D, Buonassisi T, Aziz M J and Williams J S 2017 Au-rich filamentary behavior and associated subband gap optical absorption in hyperdoped Si *Phys Rev Mater* **1** 074602

[23] Mott N F 1968 Metal-Insulator Transition *Rev Mod Phys* **40** 677–83

[24] Marti A, Cuadra L and Luque A Quantum dot intermediate band solar cell *Conference Record of the Twenty-Eighth IEEE Photovoltaic Specialists Conference - 2000 (Cat. No.00CH37036)* (IEEE) pp 940–3

[25] Rogalski A 2002 Infrared detectors: an overview *Infrared Phys Technol* **43** 187–210

[26] Rogalski A, Martyniuk P and Kopytko M 2016 Challenges of small-pixel infrared detectors: a review *Reports on Progress in Physics* **79** 046501

[27] Olea J, del Prado A, Pastor D, Mártil I and González-Díaz G 2011 Sub-bandgap absorption in Ti implanted Si over the Mott limit *J Appl Phys* **109** 113541

[28] García-Hemme E, García-Hernansanz R, Olea J, Pastor D, del Prado A, Mártil I and González-Díaz G 2014 Room-temperature operation of a titanium supersaturated silicon-based infrared photodetector *Appl Phys Lett* **104** 211105

[29] Montero Álvarez D 2021 *Near Infrared Detectors Based on Silicon Supersaturated with Transition Metals* (Cham: Springer International Publishing)

[30] Recht D, Smith M J, Charnvanichborikarn S, Sullivan J T, Winkler M T, Mathews J, Warrender J M, Buonassisi T, Williams J S, Gradečak S and Aziz M J 2013 Supersaturating silicon with transition metals by ion implantation and pulsed laser melting *J Appl Phys* **114** 124903

[31] Pastor D, Olea J, del Prado A, García-Hemme E, Mártil I, González-Díaz G, Ibáñez J, Cuscó R and Artús L 2011 UV and visible Raman scattering of ultraheavily Ti implanted Si layers for intermediate band formation *Semicond Sci Technol* **26** 115003

[32] de Unamuno S and Fogarassy E 1989 A thermal description of the melting of c- and a-silicon under pulsed excimer lasers *Appl Surf Sci* **36** 1–11

[33] Ishihara R, Yeh W-C, Hattori T and Matsumura M 1995 Effects of Light Pulse Duration on Excimer-Laser Crystallization Characteristics of Silicon Thin Films *Jpn J Appl Phys* **34** 1759–64

[34] Besaucele H, Ruet L, Adne A, Beau F, Bellier C, Ceccato P, Chatelaine M, Douri N, Dussere H, Dutems C, Heintzmann M, Huet K, Mazzamuto F, Melin A, Perrot S, Sannier O, Thebault G, Toque-Tresonne I, Zekri K, Verstraete A, Lespinasse B, Bouksou Y, Martinez V, Lenormand M and Rodrigues D 2019 High energy excimer laser system for nanosecond

annealing of semiconductor devices *XXII International Symposium on High Power Laser Systems and Applications* ed P di Lazzaro (SPIE) p 36

[35] Xu K, Vos R, Vereecke G, Lux M, Fyen W, Holsteyns F, Kenis K, Mertens P W, Heynes M M, Vinckier C and Mittal K L 2003 The haze of a wafer: A new approach to monitor nano-sized particles *PARTICLES ON SURFACES 8: DETECTION, ADHESION AND REMOVAL* (VSP BV-C/O BRILL ACAD PUBL)

[36] Acosta Alba P, Aubin J, Perrot S, Mazzamuto F, Grenier A and Kerdilès S 2021 Solid phase recrystallization induced by multi-pulse nanosecond laser annealing *Applied Surface Science Advances* **3** 100053

[37] Xu K, Vos R, Vereecke G, Lux M, Fyen W, Holsteyns F, Kenis K, Mertens P, Heyns M and Vinckier C 2003 Relation between Particle Density and Haze on a Wafer: a New Approach to Measuring Nano-Sized Particles *Solid State Phenomena* **92** 161–4

[38] Holsteyns F, Roels J, Le Q T, Kenis K and Mertens P 2004 Seeing through the haze: process monitoring and qualification using comprehensive surface data *Yield Management Solutions* **6**

[39] Luque A, Martí A, Antolín E and Tablero C 2006 Intermediate bands versus levels in non-radiative recombination *Physica B Condens Matter* **382** 320–7

[40] Pastor D, Olea J, del Prado A, García-Hemme E, García-Hernansanz R and González-Díaz G 2012 Insulator to metallic transition due to intermediate band formation in Ti-implanted silicon *Solar Energy Materials and Solar Cells* **104** 159–64

[41] Donovan E P, Spaepen F, Turnbull D, Poate J M and Jacobson D C 1983 Heat of crystallization and melting point of amorphous silicon *Appl Phys Lett* **42** 698–700

[42] Green M A 2008 Self-consistent optical parameters of intrinsic silicon at 300K including temperature coefficients *Solar Energy Materials and Solar Cells* **92** 1305–10

[43] Hishikawa Y, Nakamura N, Tsuda S, Nakano S, Kishi Y and Kuwano Y 1991 Interference-Free Determination of the Optical Absorption Coefficient and the Optical Gap of Amorphous Silicon Thin Films *Jpn J Appl Phys* **30** 1008–14

[44] Aydinly A. Topaçli C. G Y Simulation of explosive crystallisation in pulsed laser irradiated a-Si *J Appl Phys* **22** 6

[45] Gotz G 1986 Explosive crystallization processes in silicon *Applied Physics A Solids and Surfaces* **40** 29–36

[46] Lowndes D H, Pennycook S J, Jellison G E, Withrow S P and Mashburn D N 1987 Solidification of highly undercooled liquid silicon produced by pulsed laser melting of ion-implanted amorphous silicon: Time-resolved and microstructural studies *J Mater Res* **2** 648–80

[47] Thompson M O, Mayer J W, Cullis A G, Webber H C, Chew N G, Poate J M and Jacobson D C 1983 Silicon Melt, Regrowth, and Amorphization Velocities During Pulsed Laser Irradiation *Phys Rev Lett* **50** 896–9

[48] Jellison G E and Burke H H 1986 The temperature dependence of the refractive index of silicon at elevated temperatures at several laser wavelengths *J Appl Phys* **60** 841–3

[49] Auston D H, Surko C M, Venkatesan T N C, Slusher R E and Golovchenko J A 1978 Time-resolved reflectivity of ion-implanted silicon during laser annealing *Appl Phys Lett* **33** 437–40

[50] Bonafos C, Mathiot D and Claverie A 1998 Ostwald ripening of end-of-range defects in silicon *J Appl Phys* **83** 3008–17

[51] Toulemonde M, Unamuno S, Heddache R, Lampert M O, Hage-Ali M and Siffert P 1985 Time-resolved reflectivity and melting depth measurements using pulsed ruby laser on silicon *Applied Physics A Solids and Surfaces* **36** 31–6

[52] Baeri P, Reitano R, Malvezzi A M and Borghesi A 1990 Pulsed laser melting of Si-As supersaturated solid solutions *J Appl Phys* **67** 1801–4

[53] Asheghi M, Kurabayashi K, Kasnavi R and Goodson K E 2002 Thermal conduction in doped single-crystal silicon films *J Appl Phys* **91** 5079–88

[54] Fork D K, Anderson G B, Boyce J B, Johnson R I and Mei P 1996 Capillary waves in pulsed excimer laser crystallized amorphous silicon *Appl Phys Lett* **68** 2138–40

[55] Liu X, Coxon P R, Peters M, Hoex B, Cole J M and Fray D J 2014 Black silicon: fabrication methods, properties and solar energy applications *Energy Environ. Sci.* **7** 3223–63

[56] Zhao Y, Lai J, Zhou H and Yi X 2004 Fabrication of anisotropic structures with large aspect ratio and minimal roughness by using black silicon method *MEMS/MOEMS Tech & App II* ed Z Ma, G Jin and X Chen pp 196–200

[57] Pedraza A J, Fowlkes J D and Lowndes D H 1999 Silicon microcolumn arrays grown by nanosecond pulsed-excimer laser irradiation *Appl Phys Lett* **74** 2322–4

[58] Olea J, Pastor D, García-Hemme E, García-Hernansanz R, del Prado Á, Mártil I and González-Díaz G 2012 Low temperature intermediate band metallic behavior in Ti implanted Si *Thin Solid Films* **520** 6614–8

[59] Montero D, Garcia-Hernansanz R, Garcia-Hemme E, Olea J, San Andres E, del prado-Millan A and Gonzalez-Dias G 2017 Supersaturated Silicon based devices for Focal Plane Array detectors for the near and mid IR range at room temperature *11th Conference on Electron Devices* (Barcelona: IEEE)

[60] Baumann A L, Guenther K-M, Saring P, Gimpel T, Kontermann S, Seibt M and Schade W 2012 Tailoring the Absorption Properties of Black Silicon *Energy Proced* **27** 480–4

[61] Ogawa S, Kouzaki T, Yoshida T and Sinclair R 1990 Structure of the Ti-Single Crystal Si Interface *MRS Proceedings* **181** 139

[62] Moon S-J, Lee M and Grigoropoulos C P 2002 Heat Transfer and Phase Transformations in Laser Annealing of Thin Si Films *J Heat Transfer* **124** 253–64

[63] Miyasaka M and Stoemenos J 1999 Excimer laser annealing of amorphous and solid-phase-crystallized silicon films *J Appl Phys* **86** 5556–65

[64] Mathews J, Akey A J, Recht D, Malladi G, Efstathiadis H, Aziz M J and Warrender J M 2014 On the limits to Ti incorporation into Si using pulsed laser melting *Appl Phys Lett* **104** 112102

[65] Liu F, Wang M, Berencén Y, Prucnal S, Engler M, Hübner R, Yuan Y, Heller R, Böttger R, Rebohle L, Skorupa W, Helm M and Zhou S 2018 On the insulator-to-metal transition in titanium-implanted silicon *Sci Rep* **8** 4164